Optics Letters

Proposed high-speed micron-scale spatial light valve based on a silicon-graphene hybrid structure

Ciyuan Qiu,[1,*] Ting Pan,[1] Weilu Gao,[2] Ruili Liu,[1] Yikai Su,[1] and Richard Soref[3]

[1]*State Key Lab of Advanced Optical Communication Systems and Networks, Department of Electronic Engineering, Shanghai Jiao Tong University, Shanghai 200240, China*
[2]*Department of Electrical and Computer Engineering, Rice University, Houston, Texas 77005, USA*
[3]*The Engineering Program, University of Massachusetts, Boston, Massachusetts 02125, USA*
Corresponding author: qiuciyuan@sjtu.edu.cn

We propose a new ultracompact CMOS-compatible variable-transmission spatial light valve based on a silicon-graphene hybrid structure. Normally incident ∼1560 nm light can be coupled to a silicon-graphene-based 1D photonic crystal cavity through a perturbation-based diffractive coupling scheme. The lightwave modulation is achieved by tuning the Fermi level of the graphene, which can change both the loss and the resonant wavelength of the cavity. Based on finite-difference time-domain simulation, the modulation depth is larger than 10 dB with driving voltage of about 4.8 V_{pp} while the modulation speed is estimated to be higher than 45 GHz. © 2015 Optical Society of America

Spatial light modulators (SLMs) are comprised generally of a spatial array of miniature, independent, electrically addressed pixels, where each pixel is a miniature, micron-scale spatial light valve (MSLV) that has an inplane dimension of a few wavelengths in both X and Y. Previously, we reported an MSLV with a narrowband operational spectrum based on a unique silicon 1D photonic crystal (PhC) cavity [1] in which the light-valve action was described as an active dielectric antenna (ADA). High-speed SLM based on such narrowband MSLVs could be useful in optical computing [2], optical tweezer [3], and so on. In that device, the p-i-n junction was embedded across the silicon 1D PhC and was operated in the carrier injection mode. Electro-optic modulation was achieved at a speed of 150 MHz, which is limited by the relatively slow response time of the p-i-n junction. Since a p-i-n junction operated in the carrier depletion mode has a much faster response time, it is used to improve the speed of that device. However, in order to efficiently couple light into the cavity, the electrical-field distribution of the device should have a good match with that of the

input lightwave. This requires the width of the junction to be on the order of several micrometers, which makes the junction too wide for carrier depletion. Thus, it is interesting to develop a novel alternative higher-speed silicon-based MSLV by employing new structures or new materials.

Graphene, a sheet of carbon atoms in a hexagonal lattice, has attracted great interest recently in nanoscale photonic circuit research [4]. The gapless band structure of graphene with linear energy dispersion makes it strongly couple with light. In the visible-light range, graphene exhibits wavelength-independent interband absorption of ∼2.3% [4] per atomic layer. In the communication band, the interband absorption can be controlled by tuning its Fermi level (E_f) through electric gating [4]. Because graphene has such ultrawide band tunability and ultrahigh electron mobility ∼200,000 cm² V⁻¹ s⁻¹ [4], it is considered to be a promising material to build active optoelectronic devices for high-speed communications. Some near-infrared electro-optic modulators have been demonstrated based on a silicon-graphene hybrid structure, including a silicon waveguide structure [4], a PhC cavity [5,6], and a microring resonator [7,8].

By taking advantage of the ultrahigh electron mobility of graphene, we propose a high-speed MSLV based on a silicon-graphene hybrid structure. Based on finite-difference time-domain (FDTD) simulation results, the modulation depth is larger than 10 dB, while the modulation speed can reach 45 GHz, which is two orders higher than the speed of previously demonstrated ADA.

The schematic diagram of the proposed MSLV, shown in Figs. 1(a) and 1(b), is designed for the TE mode (i.e., electric field parallel to the silicon rib). The MSLV is constructed of a silicon 1D PhC cavity [1] and a graphene sheet on top. Here, the 1D PhC is formed by periodic silicon ribs on a thin silicon slab. The height of the silicon slab is 50 nm, and the height of the silicon ribs is 170 nm. The length of the silicon ribs is 4 μm (along the z direction, shown as the yellow dashed line). As shown in the cross-sectional diagram of the device [Fig. 1(b)], the Fermi level of the graphene can be tuned by applying bias
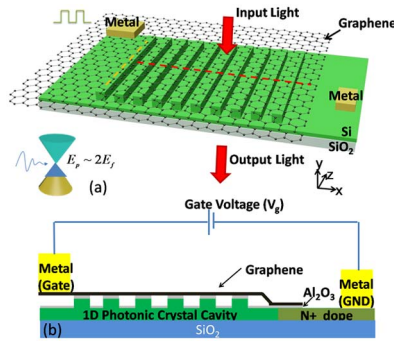
Fig. 1. (a) Diagram of the MSLV design in which the graphene is located on top of a silicon 1D PhC cavity. Lattice constant of the PhC gradually changes from 350 nm outside of the cavity to 290 nm at the center in seven periods. The dimension of the PhC in the x–z plane is 11×4 μm. The area of the device including the N+ doping slab region is about 54 μm². (b) Cross-sectional diagram of the modulator corresponding to the red dashed line in (a).

voltage between the N+ doped slab region and the graphene layer. The PhC is not doped to maintain high quality factor [7]. The device fabrication can start with a silicon on insulator (SOI) wafer having a 220 nm thick top silicon layer. The 1D PhC can be first built using electron-beam lithography and reactive ion etching (RIE). Then, doping regions are formed by patterned ion implantation. After depositing 7 nm of Al_2O_3 by atomic layer deposition (ALD), the graphene is transferred to this structure, which is then patterned by electron-beam lithography and oxygen plasma to avoid contact with the N+ doped region. Metal connection can then be formed by an electron-beam evaporator and a lift-off process.

To couple normally incident light into the Fig. 1 cavity, the cavity mode of the device is first optimized to a high quality factor by adjusting the lattice constant and thus, the bandgap, of the PhC [1]. As illustrated in Fig. 2(a), the bandgap blue-shifts and a confined cavity mode is supported if one reduces the lattice constant in the middle of the PhC rib array. The E_z distribution of the cavity mode is shown in Fig. 2(b), which has opposite signs in the neighboring ribs. Width perturbation (Δw) is then introduced by increasing the width of the silicon ribs w by Δw where $E_z > 0$ and by decreasing the width of the silicon ribs by Δw where $E_z < 0$. Here, the width perturbation (Δw) is only introduced in the PhC cavity area where the lattice constant is reduced. Then, the perturbation polarization, expressed as $\Delta \vec{P} = \Delta w \cdot \vec{E}$ [1], always points in the same direction and causes strong vertical radiation. Based on the
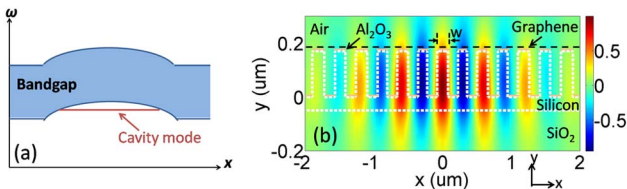
reciprocity in optics, the reverse process couples a normally incident optical beam into the resonator. Since the cavity mode has a Gaussian profile, $\Delta \vec{P}$ introduced by width perturbation also has a Gaussian profile, which maximizes the coupling efficiency for the normally incident Gaussian beam.

The normally incident light can be modulated by tuning the Fermi level of the graphene through the electric gating shown in Fig. 1(b). Here, we begin with the gate-dependent permittivity of graphene to demonstrate the principle. Gate-dependent permittivity of graphene has been extensively studied based on the random-phase approximation and the Kramers–Kronig relation. The imaginary part, ε_g'', is characterized by interband and intraband absorptions, while the real part, ε_g', can be obtained by the Kramers–Kronig relation. Thus, the gate-dependent permittivity of the graphene can be expressed as follows [9]:

$$\varepsilon_g'(E_p) = 1 + \frac{e^2}{8\pi E_p \varepsilon_0 d} \ln \frac{(E_p + 2|E_f|)^2 + \Gamma^2}{(E_p - 2|E_f|)^2 + \Gamma^2}$$
$$- \frac{e^2}{\pi \varepsilon_0 d} \frac{|E_f|}{E_p^2 + (1/\tau)^2}, \tag{1}$$

$$\varepsilon_g''(E_p) = \frac{e^2}{4 E_p \varepsilon_0 d} \left[1 + \frac{1}{\pi} \left(\tan^{-1} \frac{E_p - 2|E_f|}{\Gamma} \right. \right.$$
$$\left. \left. - \tan^{-1} \frac{E_p + 2|E_f|}{\Gamma} \right) \right] + \frac{e^2}{\pi \tau E_p \varepsilon_0 d} \frac{|E_f|}{E_p^2 + (1/\tau)^2}, \tag{2}$$

where the thickness of graphene d is set to 0.5 nm and the interband linewidth broadening Γ is set to 160 meV [7]. The free-carrier scattering rate $1/\tau$ can be neglected because it is much smaller than the incident photon energy. Figure 3(b) shows the variation of the real and imaginary parts of the permittivity under different Fermi levels at an input-light wavelength of 1560 nm. One can find the real part of the permittivity peak at $E_f = 0.4$ eV. If E_f is larger than 0.47 eV, then the sign of the real part becomes negative, and the graphene shows its metallic properties. If the Fermi level increases, the interband absorption is suppressed, and thus the imaginary part decreases.

Fig. 2. (a) Band diagram of the 1D PhC cavity as its spatial period varies along the x direction. The blue shaded area marks the bandgap. (b) E_z distribution (TE mode) corresponding to the red dashed line in (a). Here the white dashed line marks the profile of the silicon rib and slab region.
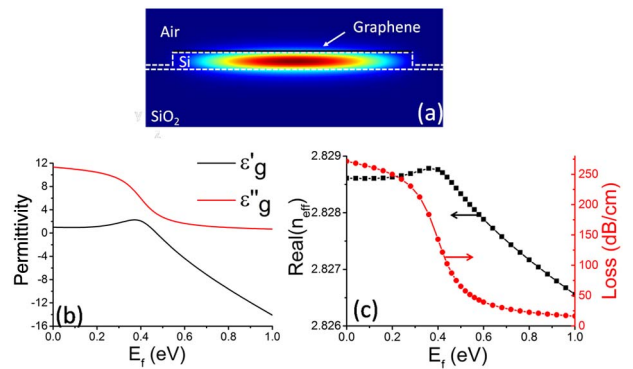
Fig. 3. (a) Electrical-field distribution at the cross section of the silicon-graphene hybrid rib corresponding to the yellow dashed line in Fig. 1(a). One can find about 0.07% power located in the graphene layer. (b) Permittivity for the graphene under different Fermi levels. (c) Real part of the effective index and loss for the silicon-graphene hybrid waveguide.

The variation of the permittivity of the graphene has a large influence on the effective index of the silicon-graphene hybrid rib (n_{eff}) because light in the silicon core is evanescently coupled to the graphene layer as shown in Fig. 3(a). The variation of n_{eff} is calculated by using the eigenmode solver of the commercial software COMSOL. As shown in Fig. 3(c), one can find the real part of n_{eff} peak at $E_f = 0.4$ eV, which agrees with the variation trend for the permittivity of the graphene. To get a better understanding of the imaginary part, it is converted to the loss of the waveguide by the wave-propagation equation as Loss $= 4.34 \times 2\pi/\lambda \times \mathrm{imag}(n_{eff})/100$. One can find that the loss of the waveguide decreases from 140 to 16 dB/cm if E_f increases from 0.4 to 1 eV. Since the resonant wavelength is determined by the real part of n_{eff} while the quality factor of the cavity mode is determined by the loss, both the resonant wavelength and the quality factor of the cavity mode can thus be changed by tuning the Fermi level. Thus electro-optic modulation can be achieved by tuning the Fermi level of the graphene.

Here, we use 2D FDTD simulation to calculate the response of the device with the geometry corresponding to the cross section located at the red dashed line shown in Fig. 1(a) [10]. The simulated transmission spectra under different Fermi levels are shown as symbols in Fig. 4. The insertion loss of the device is approximately 1 dB. If the Fermi level increases from 0.4 to 1 eV, both the real part and the imaginary parts of n_{eff} decrease. Thus, the spectrum blue-shifts while both the quality factor and the extinction ratio increase due to the suppression of the interband absorption. To study the physical process, we develop an analytical model based on the coupled-mode theory and the transfer-matrix method [1]. The device can be modeled as a multilayer dielectric structure shown in Fig. 5(a). The lth dielectric interface is described by a transfer matrix:

$$T_l = \begin{bmatrix} (n_{l-1}+n_l)/2n_l & (n_l-n_{l-1})/2n_l \\ (n_l-n_{l-1})/2n_l & (n_{l-1}+n_l)/2n_l \end{bmatrix},$$

and lth layer is described by a transfer matrix:

$$P_l = \begin{bmatrix} e^{ik_0 n_l d_l} & 0 \\ 0 & e^{-ik_0 n_l d_l} \end{bmatrix},$$

where d_l is the thickness of the lth layer and n_l is the refractive index of the lth layer. The relationship between the downward- and upward-travelling waves in the (l-1)th layer and the lth layer is thus
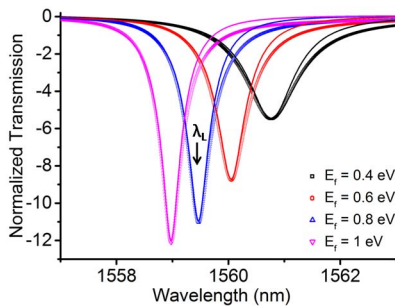
Fig. 4. Transmission spectra under different Fermi levels. The symbols are the simulation data from FDTD simulations. The solid lines are the calculated data based on coupled-mode theory. The width perturbation (Δw) for this device is 10 nm.
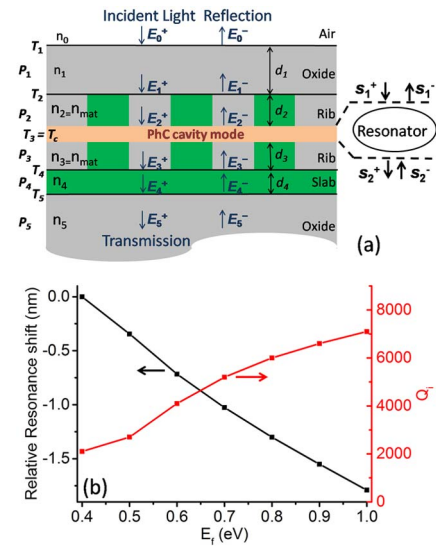
Fig. 5. (a) Diagram of the multilayer dielectric model of the MSLV. The multilayer structure is described by the transfer matrices P_l and T_l, where $1 = 1, 2 \ldots 5$. The resonant cavity is described by the transfer matrix T_c. (b) Relative resonance shift and calculated intrinsic quality variation based on coupled-mode theory.

$$\begin{pmatrix} E_l^+ \\ E_l^- \end{pmatrix} = P_l \cdot T_l \cdot \begin{pmatrix} E_{l-1}^+ \\ E_{l-1}^- \end{pmatrix},$$

where the + and – signs mark the downward- and upward-travelling waves, respectively. To model nonresonant behavior of the silicon-graphene rib array, they can be considered as a homogeneous layer with an effective index n_{mat}. Here, n_{mat} depends on the occupation ratio of the silicon ribs and the polarization of light. The resonant mode of the PhC cavity is modeled as a virtual interface in the middle of the homogeneous layer. The transfer matrix T_c for the virtual interface can be obtained from the coupled-mode theory. Since the PhC cavity mode couples to both the upward- and downward-+traveling optical beams, it can be expressed as a single-mode optical resonator coupled with two ports, as shown in the inset figure of Fig. 5(a). The dynamic equations for the amplitude of the resonance mode can be expressed as [11]

$$\frac{da}{dt} = \left[i(\omega - \omega_0) - \frac{1}{2\tau_0} - \frac{|\kappa_1|^2 + |\kappa_2|^2}{2} \right] \cdot a + \kappa_1 s_1^+ + \kappa_2 s_2^-,$$

(3)

$$s_2^+ = s_1^+ - \kappa_1^* a,$$

(4)

$$s_1^- = s_2^- - \kappa_2^* a,$$

(5)

where ω is the frequency of the input wave and ω_0 is the resonant frequency of the PhC cavity. Here s describes the amplitude of the upward or downward waves, which is normalized such that $|s|^2$ is the power of the wave. a represents the amplitude of the resonant mode, which is normalized such that $|a|^2$ is the energy in the cavity. τ_0 is the intrinsic photonic lifetime of the cavity, and it can be expressed as $\tau_0 = Q_i \lambda_0 / 2\pi c$, where Q_i is the intrinsic quality factor. Here, both the photon lifetime τ_0 and the resonant frequency ω_0 depend on the Fermi level of graphene. κ_1 and κ_2 are the field coupling coefficients, which

are associated with the downward- and upward-propagating waves. The coupling coefficients determine the coupling quality factor Q_c as

$$|\kappa_1|^2 + |\kappa_2|^2 = 2\pi c/Q_c\lambda_0. \tag{6}$$

Under the steady state ($da/dt = 0$), the amplitude a of the resonant mode can be expressed as

$$a = \frac{(k_1 s_1^+ + k_2 s_2^-)}{-i(\omega - \omega_0) + (|k_1|^2 + |k_2|^2)/2 + 1/2\tau_0}. \tag{7}$$

By plugging Eq. (7) into Eqs. (2) and (3), the transfer matrix of the resonator T_c can be obtained as

$$\begin{bmatrix} s_2^+ \\ s_2^- \end{bmatrix} = T_c \begin{bmatrix} s_1^+ \\ s_1^- \end{bmatrix}.$$

Because the propagation property of each layer and the layer interfaces is described by a (2 × 2) transfer matrix, one can use the product of these matrices to describe the behavior of the entire multilayer structure. The transmission spectra can thus be calculated, shown as the solid lines in Fig. 4. Based on the calculation, the parameters of the resonator are obtained. The coupling strengths $|\kappa_1|^2$ and $|\kappa_2|^2$ are both found to be around 3.4×10^{11} s^{-1} under different Fermi levels, and the coupling factor thus stays unchanged around 1700. The coupling efficiency between the cavity and the input light is more than 90%. As shown in Fig. 5(b), if the Fermi level increases from 0.4 to 1 eV, the intrinsic quality factor increases from 2000 to 7000 due to the suppression of interband transition. And the resonance wavelength blue-shifts about 1.8 nm since the effective index of the silicon-graphene hybrid structure decreases. Here, the coupling scheme and the analytical model could also be found in Ref. [12], which predicted its application in a modulator.

The MSLV has a narrowband operational spectrum, as shown in Fig. 4. If the operation wavelength λ_L is set to 1559.466 nm and the Fermi level (E_f) is increased from 0.4 to 0.8 eV, the modulation depth is expected to be larger than 10 dB, as shown in Fig. 4. The capacitance can be calculated to be $C = \varepsilon_0\varepsilon_r A_c/d_g = 0.1$ pF where ε_0 is the vacuum permittivity, $\varepsilon_r(= 9.34)$ is the relative permittivity of Al$_2$O$_3$, d_g ($= 7$ nm) is the thickness of the Al$_2$O$_3$ layer, and $A_c(= 10$ μm^2) is the area of the capacitor formed by the graphene and the N+ doped slab region outside of the PhC. Thus, the speed taken as $1/2\pi RC$ can be expected to be ~45 GHz by assuming R of 30 Ω [8]. The relationship between Fermi level (E_f) and applied gate voltage (V_g) can be expressed as $E_f = \hbar V_F\sqrt{\pi(\varepsilon_0\varepsilon_r/d_r q) \cdot |V_g + V_0|}$ [4,5]. Here, $V_F(= 10^6$ m/s) is the Fermi velocity, q is the charge of an electron, V_0 is the voltage offset caused by the natural

doping, which can be calculated from the initial Fermi level. If one takes the initial Fermi level as 0.4 eV [7], V_g is calculated to be 4.8 V in order to change the E_f to 0.8 eV.

Note that a beam with a waist radius of 1.5 μm is used to characterize the performance of the single MSLV. An array of MSLVs are needed if the beam size increases while the ratio of the effective area for each MSLV, calculated as the area of the cavity mode ($= 18$ μm^2) divided by the area of the device ($= 54$ μm^2), is about 33%.

In conclusion, we propose a new ultracompact CMOS-compatible voltage-controlled variable-transmission picture-element MSLV based on a silicon-graphene hybrid structure with its 1560 nm modulation depth larger than 10 dB and with its intrinsic speed estimated to be higher than 45 GHz. The physical process of the device is also analyzed based on coupled-mode theory.

REFERENCES

1. C. Y. Qiu, J. B. Chen, Y. Xia, and Q. F. Xu, Sci. Rep. **2**, 855 (2012).
2. D. E. Tamir, N. T. Shaked, P. J. Wilson, and S. Dolev, J. Opt. Soc. Am. A **26**, A11 (2009).
3. O. M. Marago, P. H. Jones, P. G. Gucciardi, G. Volpe, and A. C. Ferrari, Nat. Nanotechnol. **8**, 807 (2013).
4. M. Liu, X. B. Yin, E. Ulin-Avila, B. S. Geng, T. Zentgraf, L. Ju, F. Wang, and X. Zhang, Nature **474**, 64 (2011).
5. A. Majumdar, J. Kim, J. Vuckovic, and F. Wang, Nano Lett. **13**, 515 (2013).
6. X. T. Gan, R. J. Shiue, Y. D. Gao, K. F. Mak, X. W. Yao, L. Z. Li, A. Szep, D. Walker, J. Hone, T. F. Heinz, and D. Englund, Nano Lett. **13**, 691 (2013).
7. C. Y. Qiu, W. L. Gao, R. Vajtai, P. M. Ajayan, J. Kono, and Q. F. Xu, Nano Lett. **14**, 6811 (2014).
8. T. C. Phare, Y. D. Lee, J. Cardenas, and M. Lipson, Nat. Photonics **9**, 511 (2015).
9. J. Kim, H. Son, D. J. Cho, B. S. Geng, W. Regan, S. F. Shi, K. Kim, A. Zettl, Y. R. Shen, and F. Wang, Nano Lett. **12**, 5598 (2012).
10. B. Wang, J. H. Jiang, and G. P. Nordin, Opt. Express **12**, 3313 (2004).
11. C. Manolatou, M. J. Khan, S. H. Fan, P. R. Villeneuve, H. A. Haus, and J. D. Joannopoulos, IEEE J. Quantum Electron. **35**, 1322 (1999).
12. X. T. Gan, K. F. Mak, Y. D. Gao, Y. M. You, F. Hatami, J. Hone, T. F. Heinz, and D. Englund, Nano Lett. **12**, 5626 (2012).